

# Neighborhood-aware Geometric Encoding Network for Point Cloud Registration

Lifa Zhu<sup>1</sup> Haining Guan<sup>2</sup> Changwei Lin<sup>1</sup> Renmin Han<sup>3\*</sup>

## Abstract

The distinguishing geometric features determine the success of point cloud registration. However, most point clouds are partially overlapping, corrupted by noise, and comprised of indistinguishable surfaces, which makes it a challenge to extract discriminative features. Here, we propose the Neighborhood-aware Geometric Encoding Network (NgeNet) for accurate point cloud registration. NgeNet utilizes a geometric guided encoding module to take geometric characteristics into consideration, a multi-scale architecture to focus on the semantically rich regions in different scales, and a consistent voting strategy to select features with proper neighborhood size and reject the specious features. The awareness of adaptive neighborhood points is obtained through the multi-scale architecture accompanied by voting. Specifically, the proposed techniques in NgeNet are model-agnostic, which could be easily migrated to other networks. Comprehensive experiments on indoor, outdoor and object-centric synthetic datasets demonstrate that NgeNet surpasses all of the published state-of-the-art methods. The code will be available at <https://github.com/zhulf0804/NgeNet>.

## 1. Introduction

Point cloud registration serves as the key component in various downstream tasks such as 3D reconstruction (Geiger et al., 2011) and SLAM (Salas-Moreno et al., 2013; Zhang & Singh, 2015). Point cloud registration tries to find a transformation that best aligns two overlapping point clouds. However, due to the partial overlap, noise, and indistinguishable surfaces (planes, smooth surfaces, etc.), the robust and accurate registration of real-world point clouds remains a challenging issue.

Various methods have been proposed in previous decades.

<sup>1</sup>DeepGlint, Beijing, China; <sup>2</sup>School of Automation Science and Electrical Engineering, Beihang University, Beijing, China;

<sup>3</sup>Research Center for Mathematics and Interdisciplinary Sciences, Shandong University, Shandong, China. Correspondence to: Renmin Han <hanrenmin@sdu.edu.cn>.

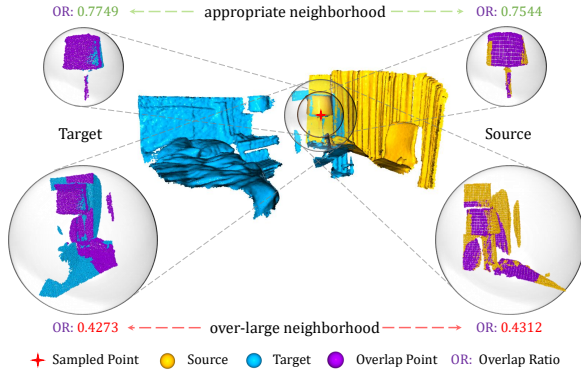


Figure 1. The neighborhood size of a sampling point affects its information representation (proportion of overlapping points) in the overlapping point cloud. If an over-large neighborhood is selected, the correlation of the corresponding points on two overlapping point clouds decrease dramatically, leading to a mismatch.

ICP (Besl & McKay, 1992) is a classic method to register two point clouds by iteratively finding correspondences and estimating pose transformation. Subsequently, several improvements (Rusinkiewicz & Levoy, 2001; Yang et al., 2015) are proposed to promote performance by searching in a larger pose space and changing objective functions. Meanwhile, hand-crafted descriptors such as FPFH (Rusu et al., 2008; 2009) and SHOT (Tombari et al., 2010) are devised to discover the local invariance in point clouds and find the pairwise correspondences to assist transformation estimation. However, to design an efficient and robust descriptor that fully utilizes the point information is non-trivial.

Recently, a number of deep learning methods have been devised for point cloud registration, which can be roughly divided into two categories: **end-to-end** learning methods and **feature-learning** based methods. The end-to-end learning methods complete both point feature learning and transformation estimation in one forward pass, some (Wang & Solomon, 2019a;b; Yew & Lee, 2020; Fu et al., 2021; Choy et al., 2020; Lee et al., 2021) of which rely on correspondences establishment for subsequent Procrustes analysis, while the others pay more attention to global features between the point clouds (Aoki et al., 2019; Sarode et al., 2019; Huang et al., 2020). In contrast, feature-learning based methods (Deng et al., 2018b;a; Gojcic et al., 2019; Choy et al., 2019; Bai et al., 2020; Huang et al., 2021; Ao et al., 2021; Yu et al., 2021) focus on the learning of discrim-

inative point features, while the 3D rigid transformation is estimated by some robust pose estimators (Fischler & Bolles, 1981; Yang et al., 2020).

Feature-learning based methods concentrate on the extraction of geometric and other useful information of the point clouds to compose discriminative features. PPFNet (Deng et al., 2018a;b) introduces PPF (Drost et al., 2010) for feature encoding. 3DSmoothNet (Gojcic et al., 2019) adopts smoothed density representations for 3D data and utilizes hierarchical 3D convolutions to get deep features. FCGF (Choy et al., 2019) utilizes a sparse 3D fully-convolutional network with metric learning to extend receptive field and extract geometric features. SpinNet (Ao et al., 2021) proposes spatial cylindrical convolutions to convert local patches into rotation-invariant features. Furthermore, some strategies are explored to boost the feature-learning based registration performance. D3Feat (Bai et al., 2020), PREDATOR (Huang et al., 2021) and CoFiNet (Yu et al., 2021) leverage the previous feature extractors (Thomas et al., 2019) by explicitly selecting salient points, overlapping points or leveraging a coarse-to-fine strategy to build correspondences. However, the neighborhood size of the features has been rarely studied. An inappropriate neighborhood of the interest point will degenerate the feature encoding (Figure 1 gives an example), while the points with small neighborhoods and locating in indistinguishable surfaces usually mislead the correspondence determination.

In this work, we propose a novel Neighborhood-aware Geometric Encoding Network (NgeNet) for accurate point cloud registration. NgeNet utilizes a multi-scale architecture to explicitly generate point-wise features with multiple neighborhood sizes and a geometric-guided encoding module to maximally utilize the geometric information. Specifically, a voting mechanism is designed to select a proper neighborhood size for each point and reject the spurious features on the indistinguishable surfaces. Experiments on indoor, outdoor and object-centric synthetic datasets show that NgeNet outperforms the classic methods in point cloud registration. Particularly, our method gains  $\sim 6\%$  and  $\sim 4\%$  performance enhancement (92.9% and 71.9% in Registration Recall) on indoor benchmarks compared with the-state-of-art methods. Furthermore, the proposed techniques are model-agnostic, able to be easily migrated to other networks.

In summary, our main contributions are as follows:

- A multi-scale architecture coupled with geometric-guided encoding to produce multi-level features encoded with geometric and semantic information.
- A multi-level consistency voting to select proper neighborhood for each point and reject the spurious ones.
- The proposed techniques in our method are model-agnostic, able to be easily migrated to other backbone architectures and improve the performance.

## 2. Related Work

### 2.1. Point cloud encoding methods

The early point descriptors (encoding) are mainly hand-crafted. 3D shape context (Tombari et al., 2010) use surface normal as a local reference frame and accumulate points in the support into discrete bins to compose a describable vector. Fast point feature histogram (FPFH) (Rusu et al., 2008; 2009) discovers point pair relationship inside the support and cast the statistical information into multi-dimensional histograms. The point pair feature (PPF) (Drost et al., 2010) discovers the relative position and orientation of two oriented points to create a global model description.

Recently, point cloud encoding based on deep learning has been widely used. PointNet (Qi et al., 2017a) and PointNet++ (Qi et al., 2017b) utilize multi-layer perceptron (MLP) and feature aggregation for point encoding. DGCNN (Wang et al., 2019) propose EdgeConv to explicitly constructs a local graph for point encoding. KPConv (Thomas et al., 2019) and FCGF (Choy et al., 2019) utilize kernel-based convolution or sparse convolution for point encoding. Based on the inherent order invariance of point clouds, Transformer methods (Vaswani et al., 2017; Guo et al., 2021; Zhao et al., 2021) employs attention for point encoding. Concurrently, the methods combining both hand-crafted and learning-based techniques have also been explored. PPFNet (Deng et al., 2018b;a), RPMNet (Yew & Lee, 2020) and ROPNet (Zhu et al., 2021) integrates hand-crafted PPF into deep learning architecture for robust point cloud registration. Nevertheless, for real-world large-scale point clouds, due to the limited GPU memory and computational resources, integrating geometric encoding into feature-learning architecture in a one-forward-pass manner (not in a patch-wise manner) is still a huge challenge.

### 2.2. Multi-scale architectures

Inspired by the great success of the various multi-scale analysis methods in classic image tasks (Yu & Koltun, 2015; Liu et al., 2016; Lin et al., 2017; Gao et al., 2019), multi-scale neural networks have been adopted in 3D point cloud tasks, including semantic segmentation (Qiu et al., 2021), object classification (Qin et al., 2019) and detection (Kuang et al., 2020). Until recently, multi-scale architecture has been employed in point cloud registration. HRegNet (Lu et al., 2021) is an end-to-end registration method that utilizes multi-scale feature maps for transformation estimation from coarse to fine. MS-SVConv (Horache et al., 2021) consumes multi-scale point clouds with different downsample voxel size for multiple features extraction, and fuse the features as the final features in a feature-learning based manner. Actually, the multi-scale features in MS-SVConv are obtained mainly based on multi-scale inputs but not a multi-scale network architecture.

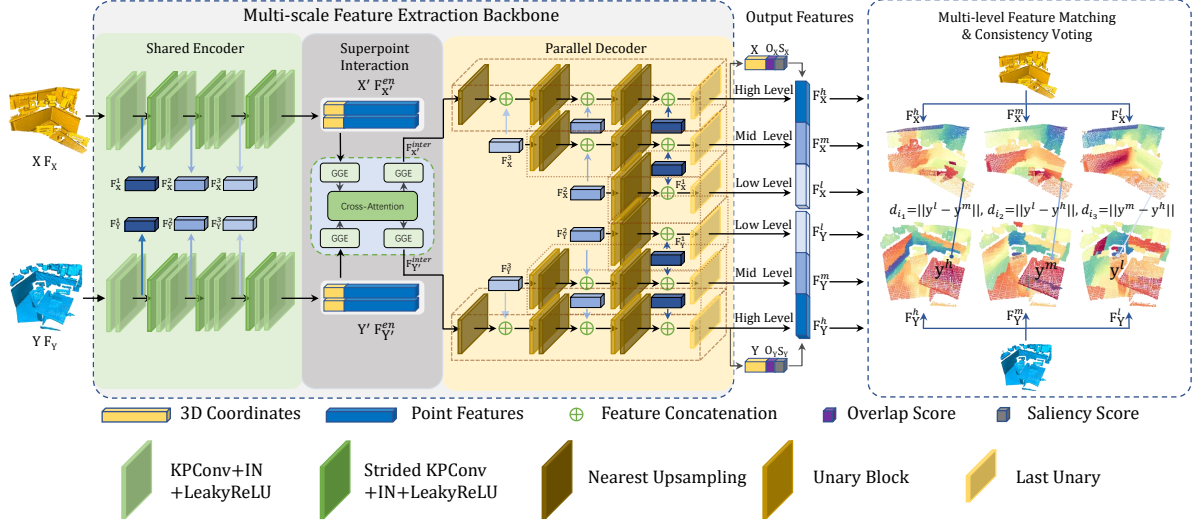


Figure 2. The architecture of NgeNet. Inputted the source and target point clouds, NgeNet utilizes siamese shared layers with a novel geometric-encoding interaction module applied to the *superpoints* to encode the information of the point clouds, and multi-scale parallel decoding layers to extract multi-level point-wise features for each point cloud. A learning-free consistency voting mechanism is designed to select the feature with the appropriate neighborhood for each point and reject the spurious features on indistinguishable surfaces.

### 3. Preliminaries

#### 3.1. Point cloud registration

Given the source point cloud  $\mathcal{X} = \{\mathbf{x}_i \in \mathbb{R}^3\}_{i=1,2,\dots,N}$  and target point cloud  $\mathcal{Y} = \{\mathbf{y}_j \in \mathbb{R}^3\}_{j=1,2,\dots,M}$ , where  $N$  and  $M$  are the point number in  $\mathcal{X}$  and  $\mathcal{Y}$ , the aim of point cloud registration is to find a transformation  $T \in \mathbf{SE}(3)$  that best aligns  $\mathcal{X}$  and  $\mathcal{Y}$ , which can be formulated as follows:

$$\arg \min_T \frac{1}{|\sigma|} \sum_{(i,j) \in \sigma} \|T(\mathbf{x}_i) - \mathbf{y}_j\|_2, \quad (1)$$

where  $\sigma$  denotes the correspondence set and  $|\cdot|$  denotes the cardinal number.

#### 3.2. Neighborhood analysis

An encoder-decoder network is usually used in a feature-learning based registration method. Generally, inputted the source point cloud  $\mathbf{X} \in \mathbb{R}^{N \times 3}$  and the target point cloud  $\mathbf{Y} \in \mathbb{R}^{M \times 3}$ , the network outputs features  $\mathbf{F}_X \in \mathbb{R}^{N \times C}$  and  $\mathbf{F}_Y \in \mathbb{R}^{M \times C}$ , with each row corresponding to  $C$ -dimensional feature of a point<sup>1</sup>. There are two ways to affect the receptive field (neighborhood size) in point convolutions. On the one hand, consecutive convolutional layers can implicitly increase the neighborhood size. Figure 3a gives out such an example, where the neighborhood size of the selected point  $\mathbf{x}_i$  is extended when the convolutional layer goes deeper. On the other hand, strided convolutional layers with the neighborhood size doubly extended are usually used in the encoder-decoder network to analogy the

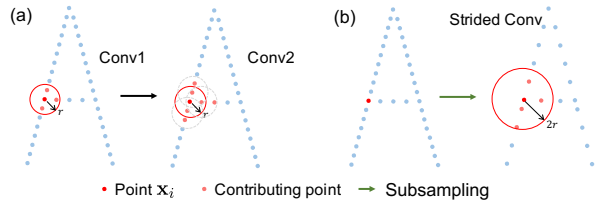


Figure 3. Illustration of the contributing neighborhood points in the point convolutions.

image downsampling in point cloud analysis, as illustrated in Figure 3b. When the network goes deeper, the receptive field of the sampled points will extend and include more structure information.

### 4. Method

#### 4.1. Network Architecture

NgeNet is an encoder-decoder network (Figure 2). The basic convolution block in the encoder consists of a residual-style KPConv / strided KPConv layer, an instance norm layer and a Leaky ReLU layer ( $k=0.1$ ). The upsampling block in the decoder adopts nearest searching for the feature interpolating. The unary block consists of a linear (MLP) layer, an instance norm layer and a Leaky ReLU layer ( $k=0.1$ ), while the last unary block just consists of a linear layer.

NgeNet takes the source point cloud  $\mathbf{X}$  and its initial descriptor  $\mathbf{F}_X$ , the target point cloud  $\mathbf{Y}$  and its initial descriptor  $\mathbf{F}_Y$  as input ( $\mathbf{F}_X$  and  $\mathbf{F}_Y$  are initialized to the matrix of ones). A siamese multi-scale backbone (subsection 4.2.1) with geometric-guided encoding (subsection 4.2.2) and information cross interaction (subsection 4.2.3) is utilized to process

<sup>1</sup>For the convenience of following discussion, all the data objects are denoted by matrix but not set.

the input data, and outputs each point cloud's corresponding high-, middle- and low-level features ( $\mathbf{F}_X^h, \mathbf{F}_X^m, \mathbf{F}_X^l$  and  $\mathbf{F}_Y^h, \mathbf{F}_Y^m, \mathbf{F}_Y^l$ ), overlap scores ( $\mathbf{O}_X$  and  $\mathbf{O}_Y$ ) and saliency scores ( $\mathbf{S}_X$  and  $\mathbf{S}_Y$ ). The specified loss function is introduced for the network training (subsection 4.3). Here, each row vector of the feature matrices represents the  $C$ -dimensional feature of a point in the point cloud. Finally, a learning-free consistent voting mechanism (subsection 4.4) is proposed to select the most discriminative feature (with proper neighborhood) for each point or reject the points on the indistinguishable smooth surfaces.

## 4.2. Main Component

### 4.2.1. SIAMESE MULTI-SCALE BACKBONE

The siamese multi-scale backbone processes the inputted point cloud  $\mathbf{X}$  and  $\mathbf{Y}$  with shared weights. Here, without loss of generality, we utilize  $\mathbf{X}$ 's part as an example to deliberate the detailed implementation of the backbone.

**Shared Encoder.** As shown in Figure 2, the encoder adopts KPConv (Thomas et al., 2019) as the basic unit. Specifically, 3 strided KPConv blocks are applied on the subsampled point clouds to extend the neighborhood in convolutions. The feature maps before each strided KPConv block are saved (denoted as  $\mathbf{F}_X^1, \mathbf{F}_X^2, \mathbf{F}_X^3$ ) for the decoder to generate multi-scale features. Here, it should be noticed that the perception range of the neighborhood points for each point feature extended from  $\mathbf{F}_X^1$  to  $\mathbf{F}_X^3$ . After the encoder, *superpoints*  $\mathbf{X}'$  and its feature  $\mathbf{F}_{X'}^{en} \in \mathbb{R}^{N' \times D_{en}}$  are obtained.

**Parallel Decoder.** The decoder accepts  $\mathbf{F}_X^1, \mathbf{F}_X^2, \mathbf{F}_X^3$  and  $\mathbf{F}_{X'}^{inter}$  (see subsection 4.2.3) as input, and outputs the high-, middle- and low-level features of the points in  $\mathbf{X}$ , i.e.,  $\mathbf{F}_X^h, \mathbf{F}_X^m, \mathbf{F}_X^l$ . For the convenience of further discussion, a basic operation is predefined as:

$$\phi(\mathbf{F}^1, \mathbf{F}^2, g) = \text{cat}[\text{Up}(g(\mathbf{F}^2)), \mathbf{F}^1], \quad (2)$$

where  $\mathbf{F}^1$  and  $\mathbf{F}^2$  are the inputted features,  $g$  is a function representing MLP or *Identity* layer,  $\text{cat}[\cdot, \cdot]$  is the concatenation operation and  $\text{Up}(\cdot)$  is the nearest upsampling. Then, the  $\mathbf{F}_X^l, \mathbf{F}_X^m$  and  $\mathbf{F}_X^h$  are calculated as follows:

$$\begin{aligned} \mathbf{F}_X^l &= \text{MLP}_2(\phi(\mathbf{F}_X^1, \mathbf{F}_X^2, \text{MLP}_1)), \\ \mathbf{F}_X^m &= \text{MLP}_5(\phi(\mathbf{F}_X^1, \phi(\mathbf{F}_X^2, \mathbf{F}_X^3, \text{MLP}_3), \text{MLP}_4)), \\ \mathbf{F}_X^h &= \text{MLP}_8(\phi(\mathbf{F}_X^1, \phi(\mathbf{F}_X^2, \phi(\mathbf{F}_X^3, \mathbf{F}_{X'}^{inter}, \text{Identity}), \\ &\quad \text{MLP}_6), \text{MLP}_7)). \end{aligned} \quad (3)$$

The details are shown in Figure 2. Additionally, the overlap scores  $\mathbf{O}_X$  and saliency scores  $\mathbf{S}_X$  are calculated along with  $\mathbf{F}_X^h$ , to provide the probability for each point in salient overlapping point sampling. However, different from PREDA-TOR (Huang et al., 2021) that focuses on the point sampling (i.e overlap and saliency scores), NgeNet pay more attention to the encoding of point features.

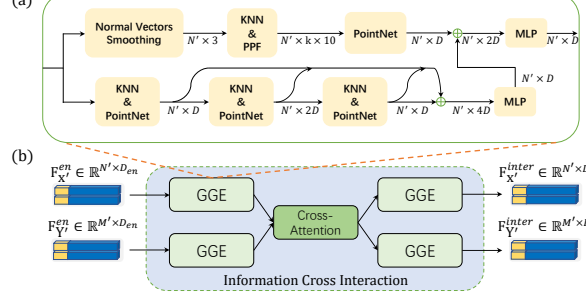


Figure 4. Geometric-guided encoding & information interaction.

### 4.2.2. GEOMETRIC-GUIDED ENCODING

Geometric-guided encoding (GGE) module takes the *superpoints* and the corresponding latent features as input, and outputs geometry enhanced features (Figure 4a).

**Normal vectors smoothing.** Normal vectors are used to enhance the geometric encoding (Rusu et al., 2008; 2009). Specifically, a smoothing strategy is proposed here to ensure the correct geometric presentation of the normal vectors in our GGE. Firstly, the subsampled superpoints  $\mathbf{X}'$  are mapped back to the original  $\mathbf{X}$ . Then, the normals  $\mathbf{N}_X$  for  $\mathbf{X}$  are calculated with Open3D's classic API (Zhou et al., 2018). Finally, the normal vector of a certain point in  $\mathbf{X}'$  is calculated by averaging the normals of its surrounding points in  $\mathbf{X}$ . That is, for point  $\mathbf{x}'_i \in \mathbf{X}'$ , the smoothed normal vector  $\mathbf{N}_{\mathbf{x}'_i}$  is calculated as

$$\mathbf{N}_{\mathbf{x}'_i} = \frac{1}{|J_i^N|} \sum_{\mathbf{x}_j \in J_i^N} \mathbf{N}_{\mathbf{x}_j}, \quad (4)$$

where  $J_i^N = \{\mathbf{x}_j \mid \|\mathbf{x}_j - \mathbf{x}'_i\| < r^N\}$ ,  $\mathbf{x}_j \in \mathbf{X}$  and  $r^N$  is the radius of  $\mathbf{x}'_i$ 's neighborhood.

**Geometric encoding.** Inspired by Yew & Lee (2020), the geometric features  $\mathbf{G}_{\mathbf{x}'_i}$  for point  $\mathbf{x}'_i \in \mathbf{X}'$  is constructed with PPF (Drost et al., 2010), i.e.,

$$\begin{aligned} \text{PPF}(\mathbf{x}'_i, \mathbf{x}'_j) &= (\angle(\mathbf{x}'_j - \mathbf{x}'_i, \mathbf{N}_{\mathbf{x}'_i}), \angle(\mathbf{x}'_j - \mathbf{x}'_i, \mathbf{N}_{\mathbf{x}'_j}), \\ &\quad \angle(\mathbf{N}_{\mathbf{x}'_i}, \mathbf{N}_{\mathbf{x}'_j}), \|\mathbf{x}'_i - \mathbf{x}'_j\|_2), \\ \mathbf{G}_{\mathbf{x}'_i} &= f_1(\mathbf{x}'_i, \mathbf{x}'_j - \mathbf{x}'_i, \text{PPF}(\mathbf{x}'_i, \mathbf{x}'_j)), \\ \mathbf{G}_{\mathbf{x}'_i} &= \max\{\mathbf{G}_{\mathbf{x}'_j} \mid \mathbf{x}'_j \in J_i^G\}. \end{aligned} \quad (5)$$

where  $\angle(\cdot, \cdot) \in [0, \pi]$  denotes the angle between the two vectors,  $f_1$  is implemented by PointNet (Qi et al., 2017a),  $J_i^G = \{\mathbf{x}'_j \mid \|\mathbf{x}'_j - \mathbf{x}'_i\| < r^G\}$ ,  $r^G$  is the radius of  $\mathbf{x}'_i$ 's neighborhood, and  $\max(\cdot)$  means channel-wise max-pooling.

**Semantic encoding.** Inspired by Huang et al. (2021), the dense connected graph network is introduced in GGE module to enhance the semantic features  $\mathbf{F}_{X'}^{en}$  (outputted from the encoder) as  $\mathbf{H}_{X'}$ , which is constructed as follows,

$$\begin{aligned} \mathbf{H}_{X'}^0 &= \mathbf{F}_{X'}^{en}, \quad \mathbf{H}_{X'}^i = \text{GNN}_i(\mathbf{H}_{X'}^{i-1}), \\ \mathbf{H}_{X'} &= \text{MLP}(\text{cat}(\mathbf{H}_{X'}^1, \mathbf{H}_{X'}^2, \mathbf{H}_{X'}^3)). \end{aligned} \quad (6)$$

Then we explicitly fuse the geometric features  $\mathbf{G}_{\mathbf{X}'}$  with the semantic features  $\mathbf{H}_{\mathbf{X}'}$  to generate our GGE features:

$$\mathbf{F}_{\mathbf{X}'}^{gge} = f_2(\mathbf{G}_{\mathbf{X}'}, \mathbf{H}_{\mathbf{X}'}), \quad (7)$$

where  $f_2$  is implemented by PointNet,  $\mathbf{F}_{\mathbf{X}'}^{gge} \in \mathbf{R}^{N' \times D}$ .

#### 4.2.3. INFORMATION CROSS INTERACTION

As shown in Figure 2, the information cross interaction module bridges the encoder and decoder, and further translates the  $\mathbf{F}_{\mathbf{X}'}^{en}$  and  $\mathbf{F}_{\mathbf{Y}'}^{en}$  to information interacted features  $\mathbf{F}_{\mathbf{X}'}^{inter}$ ,  $\mathbf{F}_{\mathbf{Y}'}^{inter}$ , which consists of two shared GGE module and one cross attention module (Figure 4b).

The cross attention is a multi-head attention with residual connection. For  $\mathbf{X}'$  and  $\mathbf{F}_{\mathbf{X}'}^{gge}$ , the information interacted feature  $\mathbf{F}_{\mathbf{X}'}^{inter}$  is calculated as

$$\begin{aligned} \text{head}_i &= \text{softmax}\left(\frac{\mathbf{Q}_i \cdot \mathbf{K}_i^T}{\sqrt{D_i}}\right) \cdot \mathbf{V}_i, \\ \mathbf{F}_{\mathbf{X}'}^{ca} &= \text{MLP}_2(\mathbf{F}_{\mathbf{X}'}^{gge} + \text{MLP}_1(\text{cat}(\text{head}_1, \dots, \text{head}_k))), \\ \mathbf{F}_{\mathbf{X}'}^{inter} &= \text{GGE}(\mathbf{X}', \mathbf{F}_{\mathbf{X}'}^{ca}) \end{aligned} \quad (8)$$

where  $\mathbf{Q}_i = \mathbf{F}_{\mathbf{X}'}^{gge} \cdot \mathbf{W}_i^{\mathbf{Q}}$ ,  $\mathbf{K}_i = \mathbf{F}_{\mathbf{Y}'}^{gge} \cdot \mathbf{W}_i^{\mathbf{K}}$ ,  $\mathbf{V}_i = \mathbf{F}_{\mathbf{Y}'}^{gge} \cdot \mathbf{W}_i^{\mathbf{V}}$  ( $\mathbf{W}_i^{\mathbf{Q}} \in \mathbb{R}^{D \times D_i}$ ,  $\mathbf{W}_i^{\mathbf{K}} \in \mathbb{R}^{D \times D_i}$ ,  $\mathbf{W}_i^{\mathbf{V}} \in \mathbb{R}^{D \times D_i}$  are learnable weights matrices),  $k$  is the number of heads,  $D_i = D/k$ , and  $\text{GGE}(\cdot, \cdot)$  is the GGE module defined in subsection 4.2.2.  $\mathbf{F}_{\mathbf{Y}'}^{inter}$  is obtained in the same way.

### 4.3. Loss function

**Feature loss.** Circle loss for feature  $\mathbf{F}_{\mathbf{X}}^h, \mathbf{F}_{\mathbf{X}}^m, \mathbf{F}_{\mathbf{X}}^l$  and  $\mathbf{F}_{\mathbf{Y}}^h, \mathbf{F}_{\mathbf{Y}}^m, \mathbf{F}_{\mathbf{Y}}^l$  are calculated with the randomly sampled corresponding pairs  $(\mathbf{X}_c, \mathbf{Y}_c)$  from  $\mathbf{X}$  and  $\mathbf{Y}$ . For example, the loss  $\mathcal{L}_{\mathbf{X}}^h(\mathbf{F})$  for  $\mathbf{F}_{\mathbf{X}}^h$  is defined as

$$\begin{aligned} \mathcal{L}_{\mathbf{X}}^h(\mathbf{F}) &= \frac{1}{L} \sum_{i=1}^L \log[1 + \sum_{\mathbf{y}_j \in \mathcal{P}_i} \exp(\gamma \alpha_{ij}^p (D_{ij}^h - \Delta p))] \\ &\quad \cdot \sum_{\mathbf{y}_k \in \mathcal{N}_i} \exp(\gamma \alpha_{ik}^n (\Delta n - D_{ik}^h))], \end{aligned} \quad (9)$$

where  $L$  is the number of sampled corresponding pairs,  $D_{ij}^h = \|\mathbf{F}_{\mathbf{x}_i}^h - \mathbf{F}_{\mathbf{y}_j}^h\|_2$ ,  $\Delta p$  and  $\Delta n$  denote positive and negative margin,  $\alpha_{ij}^p = [D_{ij}^h - \Delta p]_+$ ,  $\alpha_{ik}^n = [\Delta n - D_{ik}^h]_+$ ,  $\mathcal{P}_i$  and  $\mathcal{N}_i$  denote the matched and unmatched points in  $\mathbf{Y}_c$  for point  $\mathbf{x}_i \in \mathbf{X}_c$ , and  $\gamma$  is a scale factor. The loss  $\mathcal{L}_{\mathbf{Y}}^h(\mathbf{F})$  is defined in the same way. Then, let  $\mathcal{L}^h(\mathbf{F}) = \frac{1}{2}(\mathcal{L}_{\mathbf{X}}^h(\mathbf{F}) + \mathcal{L}_{\mathbf{Y}}^h(\mathbf{F}))$ , and so are the  $\mathcal{L}^m(\mathbf{F})$  and  $\mathcal{L}^l(\mathbf{F})$ .

**Overlap and saliency loss.** Binary cross entropy loss is adopted for  $\mathbf{O}_{\mathbf{X}}$  and  $\mathbf{S}_{\mathbf{X}}$ , i.e.,

$$\begin{aligned} \mathcal{L}_{\mathbf{X}}(\mathbf{O}) &= - \sum_{\mathbf{x}_i \in \mathbf{X}} w_i^{\mathbf{O}} [\bar{\mathbf{O}}_{\mathbf{x}_i} \log \mathbf{O}_{\mathbf{x}_i} \\ &\quad + (1 - \bar{\mathbf{O}}_{\mathbf{x}_i}) \log(1 - \mathbf{O}_{\mathbf{x}_i})], \end{aligned} \quad (10)$$

#### Algorithm 1 Consistent Voting Mechanism

**Input:**  $\mathbf{X}$  and  $\mathbf{F}_{\mathbf{X}}^h, \mathbf{F}_{\mathbf{X}}^m, \mathbf{F}_{\mathbf{X}}^l; \mathbf{Y}$  and  $\mathbf{F}_{\mathbf{Y}}^h, \mathbf{F}_{\mathbf{Y}}^m, \mathbf{F}_{\mathbf{Y}}^l$ .

**Parameter:**  $d$ : parameter related to points density

**Output:**  $\mathbf{F}_{\mathbf{X}}^{fin}$  for  $\mathbf{X}$  and  $\mathbf{F}_{\mathbf{Y}}^{fin}$  for  $\mathbf{Y}$ .

```

1: for all  $\mathbf{x}_i \in \mathbf{X}$  do
2:   Find  $\mathbf{y}^l = NN_{\mathbf{F}^l}(\mathbf{x}_i, \mathbf{Y})$ ,  $\mathbf{y}^m = NN_{\mathbf{F}^m}(\mathbf{x}_i, \mathbf{Y})$ ,  $\mathbf{y}^h = NN_{\mathbf{F}^h}(\mathbf{x}_i, \mathbf{Y})$ 
3:   Compute  $d_{i_1} = \|\mathbf{y}^l - \mathbf{y}^m\|_2, d_{i_2} = \|\mathbf{y}^l - \mathbf{y}^h\|_2, d_{i_3} = \|\mathbf{y}^m - \mathbf{y}^h\|_2$ 
4:   if  $d_{i_2} < d$  or  $d_{i_3} < d$  then
5:      $\mathbf{F}_{\mathbf{x}_i}^{fin} = \mathbf{F}_{\mathbf{x}_i}^h, \mathbf{F}_{\mathbf{y}^h}^{fin} = \mathbf{F}_{\mathbf{y}^h}^h$ 
6:   else if  $d_{i_1} < d$  then
7:      $\mathbf{F}_{\mathbf{x}_i}^{fin} = \mathbf{F}_{\mathbf{x}_i}^m, \mathbf{F}_{\mathbf{y}^m}^{fin} = \mathbf{F}_{\mathbf{y}^m}^m$ 
8:   else
9:      $\mathbf{F}_{\mathbf{x}_i}^{fin} = null$ 
10:  end if
11: end for

```

$$\begin{aligned} \mathcal{L}_{\mathbf{X}}(\mathbf{S}) &= - \sum_{\mathbf{x}_i \in \mathbf{X}} w_i^{\mathbf{S}} [\bar{\mathbf{S}}_{\mathbf{x}_i} \log \mathbf{S}_{\mathbf{x}_i} \\ &\quad + (1 - \bar{\mathbf{S}}_{\mathbf{x}_i}) \log(1 - \mathbf{S}_{\mathbf{x}_i})], \end{aligned} \quad (11)$$

where  $w_i^{\mathbf{O}}$  and  $w_i^{\mathbf{S}}$  are weighting factors for samples balance,  $\bar{\mathbf{O}}_{\mathbf{x}_i}$  and  $\bar{\mathbf{S}}_{\mathbf{x}_i} \in \{0, 1\}$  are the ground truth binary overlap score and saliency score.  $\bar{\mathbf{O}}_{\mathbf{x}_i}$  is set to 1 if the distance between  $T^*(\mathbf{x}_i)$  and  $NN(T^*(\mathbf{x}_i), \mathbf{Y})$  is below the threshold, where  $T^*$  is the ground truth transformation and  $NN(\mathbf{x}, \mathbf{Y})$  operator reports the nearest neighbor of  $\mathbf{x}$  in  $\mathbf{Y}$ .  $\bar{\mathbf{S}}_{\mathbf{x}_i}$  is set to 1 if the ground truth candidate point is matched for  $\mathbf{x}_i$  based on feature matching (see A.2.5).  $\mathcal{L}_{\mathbf{Y}}(\mathbf{O})$  and  $\mathcal{L}_{\mathbf{Y}}(\mathbf{S})$  are defined in the same way. Then, let  $\mathcal{L}(\mathbf{O}) = \frac{1}{2}(\mathcal{L}_{\mathbf{X}}(\mathbf{O}) + \mathcal{L}_{\mathbf{Y}}(\mathbf{O}))$ ,  $\mathcal{L}(\mathbf{S}) = \frac{1}{2}(\mathcal{L}_{\mathbf{X}}(\mathbf{S}) + \mathcal{L}_{\mathbf{Y}}(\mathbf{S}))$ .

**Combined loss.** The complete loss function of NgeNet is

$$\mathcal{L} = \mathcal{L}^h(\mathbf{F}) + \mathcal{L}^m(\mathbf{F}) + \mathcal{L}^l(\mathbf{F}) + \mathcal{L}(\mathbf{O}) + \mathcal{L}(\mathbf{S}). \quad (12)$$

### 4.4. Consistent voting

Generally, an overlapping point with discriminative geometric structures is able to correctly match its corresponding point in another point cloud by features of different levels' neighborhood. Figure 5 shows such an example, where  $\mathbf{x}_1$ 's candidate points obtained from low-, middle-, high-level's feature matching are consistent, and  $\mathbf{x}_2$ 's consistency exists in both low and middle feature levels, while  $\mathbf{x}_3$  get three different candidates with different level's feature matching.

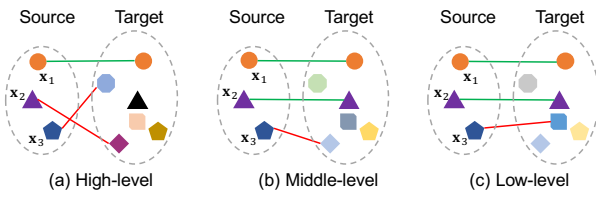


Figure 5. Multi-level consistency.

Table 1. Results on 3DMatch and 3DLoMatch under different numbers of sampling points.

# Samples	3DMatch					3DLoMatch					
	5000	2500	1000	500	250	5000	2500	1000	500	250	# Params ↓
<i>Registration Recall (%) ↑</i>											
3DSN	78.4	76.2	71.4	67.6	50.8	33.0	29.0	23.3	17.0	11.0	10.2M
FCGF	85.1	84.7	83.3	81.6	71.4	40.1	41.7	38.2	35.4	26.8	8.76M
D3Feat	81.6	84.5	83.4	82.4	77.9	37.2	42.7	46.9	43.8	39.1	27.3M
PREDATOR	89.0	89.9	90.6	88.5	86.6	59.8	61.2	62.4	60.8	58.1	7.43M
CoFiNet	89.3	88.9	88.4	87.4	87.0	67.5	66.2	64.2	63.1	61.0	5.48M
NgeNet (ours)	<b>92.9</b>	<b>92.1</b>	<b>92.3</b>	<b>90.3</b>	<b>88.7</b>	<b>71.9</b>	<b>71.4</b>	<b>70.6</b>	<b>67.5</b>	<b>61.9</b>	8.86M
<i>Feature Matching Recall (%) ↑</i>											
3DSN	95.0	94.3	92.9	90.1	82.9	63.6	61.7	53.6	45.2	34.2	10.2M
FCGF	97.4	97.3	97.0	96.7	96.6	76.6	75.4	74.2	71.7	67.3	8.76M
D3Feat	95.6	95.4	94.5	94.1	93.1	67.3	66.7	67.0	66.7	66.5	27.3M
PREDATOR	96.6	96.6	96.5	96.3	96.5	78.6	77.4	76.3	75.7	75.3	7.43M
CoFiNet	98.1	98.3	<b>98.1</b>	98.2	<b>98.3</b>	83.1	83.5	83.3	83.1	82.6	5.48M
NgeNet (ours)	<b>98.2</b>	<b>98.4</b>	<b>98.1</b>	<b>98.6</b>	98.2	<b>84.5</b>	<b>84.8</b>	<b>85.0</b>	<b>85.3</b>	<b>83.4</b>	8.86M
<i>Inlier Ratio (%) ↑</i>											
3DSN	36.0	32.5	26.4	21.5	16.4	11.4	10.1	8.0	6.4	4.8	10.2M
FCGF	56.8	54.1	48.7	42.5	34.1	21.4	20.0	17.2	14.8	11.6	8.76M
D3Feat	39.0	38.8	40.4	41.5	41.8	13.2	13.1	14.0	14.6	15.0	27.3M
PREDATOR	58.0	58.4	57.1	54.1	49.3	26.7	28.1	28.3	27.5	25.8	7.43M
CoFiNet	49.8	51.2	51.9	52.2	<b>52.2</b>	24.4	25.9	26.7	26.8	26.9	5.48M
NgeNet (ours)	<b>63.1</b>	<b>63.5</b>	<b>61.5</b>	<b>57.6</b>	51.1	<b>31.8</b>	<b>33.3</b>	<b>33.5</b>	<b>31.9</b>	<b>29.2</b>	8.86M

Thus, a simple yet effective consistent voting algorithm is proposed to select the points with the most discriminative features, which is deliberated in Algorithm 1, where the  $NN_F(\mathbf{x}, \mathbf{Y})$  operator reports the nearest neighbor of  $\mathbf{x}$  in  $\mathbf{Y}$  in feature  $\mathbf{F}$ 's space. The consistent voting process accepts the target and source point cloud  $\mathbf{X}$  and  $\mathbf{Y}$ , and their multi-level features  $\mathbf{F}_X^h, \mathbf{F}_X^m, \mathbf{F}_X^l$  and  $\mathbf{F}_Y^h, \mathbf{F}_Y^m, \mathbf{F}_Y^l$  as input, and outputs the final feature  $\mathbf{F}_X^{fin}$  for  $\mathbf{X}$  and  $\mathbf{F}_Y^{fin}$  for  $\mathbf{Y}$ . Taking  $\mathbf{x}_i$  as an example, consistent voting helps  $\mathbf{x}_i$  to select the proper feature among  $\{\mathbf{F}_{\mathbf{x}_i}^h, \mathbf{F}_{\mathbf{x}_i}^m, \mathbf{F}_{\mathbf{x}_i}^l, null\}$  as its final feature  $\mathbf{F}_{\mathbf{x}_i}^{fin}$ , where  $null$  means  $\mathbf{x}_i$  is a bad point and should not be used for correspondence building.

## 5. Experiments

NgeNet was evaluated on 3DMatch (Zeng et al., 2017), 3DLoMatch (Huang et al., 2021), Odometry KITTI (Geiger et al., 2012) and MVP-RG (Pan et al., 2021) datasets, resulting in a detailed quantitative analysis.

### 5.1. Implementation details

NgeNet was implemented in PyTorch (Paszke et al., 2019), with knn parameter  $k$  of PPF set to 64, the dimension  $D$  of  $\mathbf{F}^{gge}$  set to 256 and the dimension  $C$  of  $\mathbf{F}^{fin}$  set to 32. Parameter  $d$  in voting was set to  $2 \times$  voxel size. All experiments were conducted on a single RTX 3090 GPU. SGD optimizer with 0.98 momentum was used for network training, with initial learning rate set to 0.01 and the number of sampled point pairs  $L$  set to 256, 512 and 768 for 3DMatch (3DLoMatch), Odometry KITTI and MVP-RG, respectively. The scale factor  $\gamma$ , positive and negative margin  $\Delta p, \Delta n$

in loss function were set to 16, 0.1 and 1.4. For 3DMatch (3DLoMatch), Odometry KITTI and MVP-RG, the model was trained by 40, 150 and 200 epochs, respectively. Exponential decay was set to 0.95 after every epoch.

### 5.2. 3DMatch and 3DLoMatch

3DMatch (Zeng et al., 2017) and 3DLoMatch (Huang et al., 2021) are two widely used indoor datasets that contain  $>30\%$  and  $10 \sim 30\%$  partial overlapping scene pairs, respectively. In consistent with Huang et al. (2021), 46 scenes (20642 scan pairs) were used for training and 8 scenes (1331 scan pairs) were used for validation. 8 scenes (1279 and 1726 non-consecutive pairs for 3DMatch and 3DLoMatch) were used for testing. The *Inlier Ratio* (IR), *Feature Matching Recall* (FMR) and *Registration Recall* (RR) for each dataset were reported (The metric details are given in A.1.1).

#### 5.2.1. PERFORMANCE

NgeNet was compared with the SOTA method 3DSN (Ganjic et al., 2019), FCGF (Choy et al., 2019), D3Feat (Bai et al., 2020), PREDATOR (Huang et al., 2021) and CoFiNet (Yu et al., 2021) on 3DMatch and 3DLoMatch datasets, whose results are summarized in Table 1.

As shown in Table 1, NgeNet outperforms all the other models on both two datasets. NgeNet achieved 92.9% and 71.9% RR on 3DMatch and 3DLoMatch, exceeding PREDATOR (90.6% and 62.4% RR on 3DMatch) by 5.9% and CoFiNet (89.3% and 67.5% RR on 3DLoMatch) by 4%. Moreover, NgeNet performs the best under various number of sampling points, demonstrating the robustness of the model.

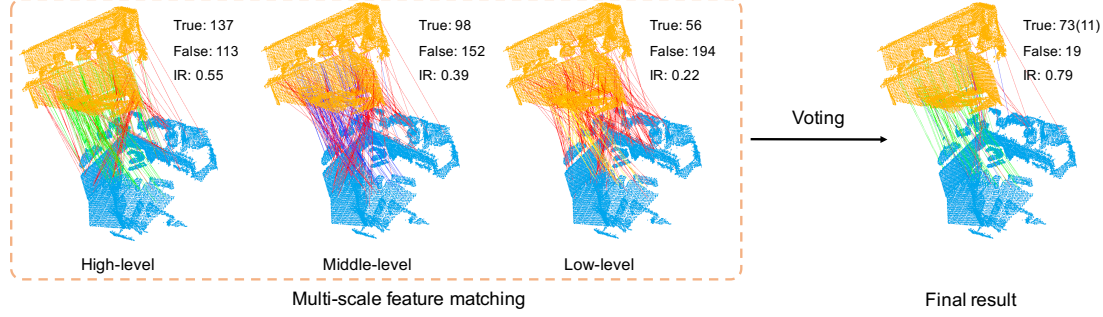


Figure 6. Correspondences constructed by multi-scale feature matching and consistent voting. 250 correspondences are randomly selected for convenience of visualization. Here, the correct correspondences obtained based on high-, middle- and low-level features are marked in green, blue and yellow, respectively. The incorrect correspondences are marked in red. The correspondences constructed from the voted neighborhood-aware features contain 11 points with middle-level features and 62 points with high-level features, having preserved most of the correct ones and rejected most of the specious features.

Furthermore, though NgeNet achieves a great performance improvement, its parameter number (8.86M) remains moderate among all the methods. Several difficult cases and failed cases can be found in Figure A2 and A3.

#### 5.2.2. NEIGHBORHOOD-AWARE FEATURES

**Influence of voting.** Figure 6 shows an example of how consistent voting works. Consistent voting assigns the most discriminative feature of the high-, middle-, and low-level features to each point, which results in the pruning of massive mismatched correspondence and reserving the correct ones (green and blue lines).

**Matched points distribution.** Figure 7 gives an example of the correctly matched points distribution on the overlap boundary and plane regions. As depicted in Figure 7a, the number of matched points with high-level features is less than that with middle- and low-level features on the boundary of overlap regions, indicating that an over-large neighborhood cannot produce discriminative features. Besides, as depicted in Figure 7b, there are few matched points on the plane surface, no matter the level of features. The phenomenon indicates that points on the plane surfaces are indistinguishable, most of which will be discarded in multi-scale feature matching and consistent voting.

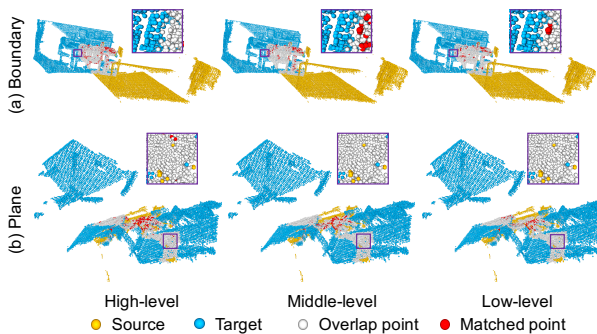


Figure 7. Matched points distribution on boundary and plane surface with multi-level features.

Table 2. Ablation study on 3DMatch.

base	ms	voting	GGE	IR (%) $\uparrow$	FMR (%) $\uparrow$	RR (%) $\uparrow$
✓				50.3	96.3	89.3
✓	✓			56.6	97.2	90.3
✓	✓	✓		60.8	98.1	91.5
✓			✓	54.4	97.4	91.2
✓	✓	✓	✓	<b>63.1</b>	<b>98.2</b>	<b>92.9</b>

#### 5.2.3. ABLATION STUDY

Multi-scale architecture (ms), consistent voting (voting) and GGE modules are the three cornerstones of NgeNet. Here, ablation study was conducted on 3DMatch dataset under 5000 sampling points, where the NgeNet without ms, voting and GGE modules was considered as the base model. Table 2 summarizes the results of the ablation study, from which we can draw the conclusion that ms+voting promotes RR by 2.2%, GGE promotes RR by 1.9% and ms+voting+GGE promotes RR by 3.6%. To our surprise, training the network with multi-levels but only testing with high-level features (base+ms) also improves the RR by 1.0%.

Table 3. Feature comparison with PREDATOR on 3DMatch.

Model	sampling	IR (%) $\uparrow$	FMR (%) $\uparrow$	RR (%) $\uparrow$
PREDATOR	random	51.6	96.5	86.0
NgeNet (ours)	random	<b>54.2</b>	<b>97.8</b>	<b>90.1</b>
PREDATOR	prob.	58.0	96.6	89.0
NgeNet (ours)	prob.	<b>63.1</b>	<b>98.2</b>	<b>92.9</b>

#### 5.2.4. FEATURES COMPARISON

The features outputted by NgeNet were compared with the ones of PREDATOR on registration task under different sampling strategies, whose experimental results are summarized in Table 3. Here, the points were either randomly sampled (*random*) or sampled based on overlap and saliency score (*prob.*). As shown in Table 3, NgeNet exceeds PREDATOR in IR, FMR and RR under both *random* and *prob.* sampling strategies, demonstrating that the features of Ngenet are more distinctive for registration. The FMR curve shown in Figure 8 demonstrates that the features of NgeNet are

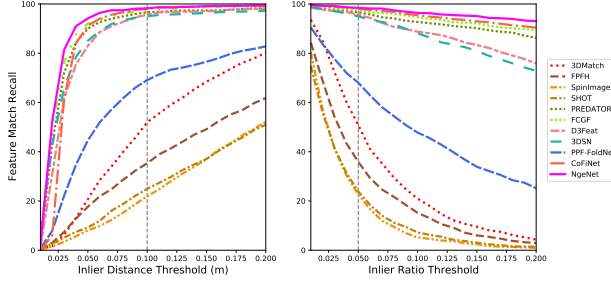


Figure 8. Feature matching recall in relation to inlier distance threshold  $\tau_1$  (left) and inlier ratio threshold  $\tau_2$  (right).

consistently better than the other methods under different thresholds  $\tau_1$  and  $\tau_2$ .

### 5.2.5. FLEXIBILITY AND EFFECTIVENESS

The flexibility and effectiveness of the proposed multi-scale architecture, consistent voting and GGE modules were validated by transferring them to other encoder-decoder architectures, such as FCGF (Choy et al., 2019), D3Feat (Bai et al., 2020) and PREDATOR (Huang et al., 2021). An experiment has been conducted on the 3DMatch, and the results are shown in Table 4. Here, it can be found that NgeNet’s modules greatly improve the baseline methods’ performance.

Table 4. Results of transferring NgeNet’s modules to other networks. The results reported in the published papers and the improvements are shown in brackets.

Model	IR (%) $\uparrow$	FMR (%) $\uparrow$	RR (%) $\uparrow$
FCGF	46.3 (56.8)	94.9 (97.4)	85.0 (85.1)
FCGF + ms + voting	<b>56.8</b> (+0.0)	<b>97.8</b> (+0.4)	89.8 (+4.7)
FCGF + ms + voting + GGE	51.5 (-5.3)	95.9 (-1.5)	<b>90.6</b> (+5.5)
D3Feat	42.9 (39.0)	95.9 (95.6)	83.2 (81.6)
D3Feat + ms + voting	48.9 (+9.9)	97.1 (+1.5)	87.0 (+5.4)
D3Feat + ms + voting + GGE	<b>49.3</b> (+10.3)	<b>97.2</b> (+1.6)	87.7 (+6.1)
PREDATOR	54.3 (58.0)	97.1 (96.6)	89.0 (89.0)
PREDATOR + ms + voting	60.0 (+2.0)	98.3 (+1.7)	89.7 (+0.7)
PREDATOR + ms + voting + GGE	<b>62.5</b> (+4.5)	<b>98.7</b> (+2.1)	<b>90.7</b> (+1.7)

## 5.3. Odometry KITTI

Odometry KITTI (Geiger et al., 2012) is an outdoor LIDAR dataset for autonomous driving. In consistent with Huang et al. (2021), the frame pair at most 10 meters were selected to form scan pairs. Then, the model was trained with sequence No.00-05 (1358 scan pairs), validated with sequence No.06-07 (180 scan pairs) and tested with sequence No.08-10 (555 pairs). Finally, the *Relative Translation Error* (RTE), *Relative Rotation Error* (RRE) and *Registration Recall* (RR) (see A.1.2) of the results are reported.

### 5.3.1. PERFORMANCE

NgeNet was compared with the SOTA method 3DFeat-Net (Yew & Lee, 2018), FCGF (Choy et al., 2019), D3Feat (Bai et al., 2020), PREDATOR (Huang et al., 2021) and CoFiNet (Yu et al., 2021), whose results are summarized in Table 5. Here, NgeNet achieve the best RR (99.8%), RTE

Table 5. Results on Odometry KITTI dataset.

Method	RTE (cm) $\downarrow$	RRE ( $^{\circ}$ ) $\downarrow$	RR (%) $\uparrow$
3DFeat-Net	25.9	0.57	96.0
FCGF	9.5	0.30	96.6
D3Feat	7.2	0.30	<b>99.8</b>
PREDATOR	6.8	0.27	<b>99.8</b>
CoFiNet	8.5	0.41	<b>99.8</b>
NgeNet (wo. GGF) ( <i>ours</i> )	<b>6.3</b>	<b>0.25</b>	<b>99.8</b>
NgeNet ( <i>ours</i> )	<b>6.1</b>	0.26	<b>99.8</b>

(6.1cm) and RRE (0.26 $^{\circ}$ ). It should be noted that NgeNet can achieve better RRE with 0.25 $^{\circ}$  without GGE module. Maybe normal vectors are not suitable for LIDAR dataset, which has relative weak structure information.

## 5.4. MVP-RG

MVP(multi-view partial)-RG dataset (Pan et al., 2021) is constructed by 16 categories object-centric synthetic point cloud. The density and unrestricted rotations ([0 $^{\circ}$ , 360 $^{\circ}$ ]) vary in different point cloud. Following Pan et al. (2021), we report three metrics  $\mathcal{L}_R$ ,  $\mathcal{L}_t$ , and  $\mathcal{L}_{RMSE}$  (see A.1.3). We used the official training set (6400 pairs) for training and used the official test set (1200 pairs) for testing.

### 5.4.1. PERFORMANCE

NgeNet was compared with PREDATOR (Huang et al., 2021), and the recent end-to-end learning-based registration methods DCP (Wang & Solomon, 2019a), RPM-Net (Yew & Lee, 2020), RGM (Fu et al., 2021) and GMCNet (Pan et al., 2021). For PREDATOR and NgeNet, both 768 correspondences were sampled for RANSAC. Table 6 summarizes the results, where NgeNet outperforms all the other methods. Particularly, NgeNet surpasses the end-to-end learning method in a remarkable margin.

Table 6. Results on MVP-RG.

Method	$\mathcal{L}_R$ ( $^{\circ}$ ) $\downarrow$	$\mathcal{L}_t$ $\downarrow$	$\mathcal{L}_{RMSE}$ $\downarrow$
DCP	30.73	0.273	0.634
RPM-Net	22.20	0.174	0.327
RGM	41.27	0.425	0.583
PREDATOR	<b>10.58</b>	<b>0.067</b>	<b>0.125</b>
GMCNet	16.57	0.174	0.246
NgeNet ( <i>ours</i> )	<b>7.99</b>	<b>0.048</b>	<b>0.093</b>

## 6. Conclusion

In this paper, we proposed NgeNet, a multi-scale encoder-decoder network combined with geometric guided encoding and a consistent voting to produce neighborhood-aware discriminative features for accurate point cloud registration. Comprehensive experiments demonstrate the efficiency and effectiveness of NgeNet. Especially, the proposed techniques in NgeNet can be transferred to other networks to expediently boost the baseline performance. In future, long-range geometric relationship and point sampling strategies will be further discussed and coupled with our neighborhood-aware features.

## References

Ao, S., Hu, Q., Yang, B., Markham, A., and Guo, Y. Spinnet: Learning a general surface descriptor for 3d point cloud registration. In *Proceedings of the IEEE/CVF Conference on Computer Vision and Pattern Recognition*, pp. 11753–11762, 2021.

Aoki, Y., Goforth, H., Srivatsan, R. A., and Lucey, S. Pointnetlk: Robust & efficient point cloud registration using pointnet. In *Proceedings of the IEEE/CVF Conference on Computer Vision and Pattern Recognition*, pp. 7163–7172, 2019.

Bai, X., Luo, Z., Zhou, L., Fu, H., Quan, L., and Tai, C.-L. D3feat: Joint learning of dense detection and description of 3d local features. In *Proceedings of the IEEE/CVF Conference on Computer Vision and Pattern Recognition*, pp. 6359–6367, 2020.

Besl, P. J. and McKay, N. D. Method for registration of 3-d shapes. In *Sensor fusion IV: control paradigms and data structures*, volume 1611, pp. 586–606. International Society for Optics and Photonics, 1992.

Choy, C., Park, J., and Koltun, V. Fully convolutional geometric features. In *Proceedings of the IEEE/CVF International Conference on Computer Vision*, pp. 8958–8966, 2019.

Choy, C., Dong, W., and Koltun, V. Deep global registration. In *Proceedings of the IEEE/CVF conference on computer vision and pattern recognition*, pp. 2514–2523, 2020.

Deng, H., Birdal, T., and Ilic, S. Ppf-foldnet: Unsupervised learning of rotation invariant 3d local descriptors. In *Proceedings of the European Conference on Computer Vision (ECCV)*, pp. 602–618, 2018a.

Deng, H., Birdal, T., and Ilic, S. Ppfnet: Global context aware local features for robust 3d point matching. In *Proceedings of the IEEE conference on computer vision and pattern recognition*, pp. 195–205, 2018b.

Drost, B., Ulrich, M., Navab, N., and Ilic, S. Model globally, match locally: Efficient and robust 3d object recognition. In *2010 IEEE computer society conference on computer vision and pattern recognition*, pp. 998–1005. Ieee, 2010.

Fischler, M. A. and Bolles, R. C. Random sample consensus: a paradigm for model fitting with applications to image analysis and automated cartography. *Communications of the ACM*, 24(6):381–395, 1981.

Fu, K., Liu, S., Luo, X., and Wang, M. Robust point cloud registration framework based on deep graph matching. In *Proceedings of the IEEE/CVF Conference on Computer Vision and Pattern Recognition*, pp. 8893–8902, 2021.

Gao, S., Cheng, M.-M., Zhao, K., Zhang, X.-Y., Yang, M.-H., and Torr, P. H. Res2net: A new multi-scale backbone architecture. *IEEE transactions on pattern analysis and machine intelligence*, 2019.

Geiger, A., Ziegler, J., and Stiller, C. Stereoscan: Dense 3d reconstruction in real-time. In *2011 IEEE intelligent vehicles symposium (IV)*, pp. 963–968. Ieee, 2011.

Geiger, A., Lenz, P., and Urtasun, R. Are we ready for autonomous driving? the kitti vision benchmark suite. In *2012 IEEE conference on computer vision and pattern recognition*, pp. 3354–3361. IEEE, 2012.

Gojcic, Z., Zhou, C., Wegner, J. D., and Wieser, A. The perfect match: 3d point cloud matching with smoothed densities. In *Proceedings of the IEEE/CVF Conference on Computer Vision and Pattern Recognition*, pp. 5545–5554, 2019.

Guo, M.-H., Cai, J.-X., Liu, Z.-N., Mu, T.-J., Martin, R. R., and Hu, S.-M. Pct: Point cloud transformer. *Computational Visual Media*, 7(2):187–199, 2021.

Horache, S., Deschaud, J.-E., and Goulette, F. 3d point cloud registration with multi-scale architecture and self-supervised fine-tuning. *arXiv preprint arXiv:2103.14533*, 2021.

Huang, S., Gojcic, Z., Usvyatsov, M., Wieser, A., and Schindler, K. Predator: Registration of 3d point clouds with low overlap. In *Proceedings of the IEEE/CVF Conference on Computer Vision and Pattern Recognition*, pp. 4267–4276, 2021.

Huang, X., Mei, G., and Zhang, J. Feature-metric registration: A fast semi-supervised approach for robust point cloud registration without correspondences. In *Proceedings of the IEEE/CVF Conference on Computer Vision and Pattern Recognition*, pp. 11366–11374, 2020.

Kuang, H., Wang, B., An, J., Zhang, M., and Zhang, Z. Voxel-fpn: Multi-scale voxel feature aggregation for 3d object detection from lidar point clouds. *Sensors*, 20(3):704, 2020.

Lee, J., Kim, S., Cho, M., and Park, J. Deep hough voting for robust global registration. In *Proceedings of the IEEE/CVF International Conference on Computer Vision*, pp. 15994–16003, 2021.

Lin, T.-Y., Dollár, P., Girshick, R., He, K., Hariharan, B., and Belongie, S. Feature pyramid networks for object detection. In *Proceedings of the IEEE conference on computer vision and pattern recognition*, pp. 2117–2125, 2017.

Liu, W., Anguelov, D., Erhan, D., Szegedy, C., Reed, S., Fu, C.-Y., and Berg, A. C. Ssd: Single shot multibox detector. In *European conference on computer vision*, pp. 21–37. Springer, 2016.

Lu, F., Chen, G., Liu, Y., Zhang, L., Qu, S., Liu, S., and Gu, R. Hregnet: A hierarchical network for large-scale outdoor lidar point cloud registration. In *Proceedings of the IEEE/CVF International Conference on Computer Vision*, pp. 16014–16023, 2021.

Pan, L., Cai, Z., and Liu, Z. Robust partial-to-partial point cloud registration in a full range. *arXiv preprint arXiv:2111.15606*, 2021.

Paszke, A., Gross, S., Massa, F., Lerer, A., Bradbury, J., Chanan, G., Killeen, T., Lin, Z., Gimelshein, N., Antiga, L., et al. Pytorch: An imperative style, high-performance deep learning library. *Advances in neural information processing systems*, 32:8026–8037, 2019.

Qi, C. R., Su, H., Mo, K., and Guibas, L. J. Pointnet: Deep learning on point sets for 3d classification and segmentation. In *Proceedings of the IEEE conference on computer vision and pattern recognition*, pp. 652–660, 2017a.

Qi, C. R., Yi, L., Su, H., and Guibas, L. J. Pointnet++: Deep hierarchical feature learning on point sets in a metric space. *arXiv preprint arXiv:1706.02413*, 2017b.

Qin, C., You, H., Wang, L., Kuo, C.-C. J., and Fu, Y. Pointdan: A multi-scale 3d domain adaption network for point cloud representation. *arXiv preprint arXiv:1911.02744*, 2019.

Qiu, S., Anwar, S., and Barnes, N. Semantic segmentation for real point cloud scenes via bilateral augmentation and adaptive fusion. In *Proceedings of the IEEE/CVF Conference on Computer Vision and Pattern Recognition*, pp. 1757–1767, 2021.

Rusinkiewicz, S. and Levoy, M. Efficient variants of the icp algorithm. In *Proceedings third international conference on 3-D digital imaging and modeling*, pp. 145–152. IEEE, 2001.

Rusu, R. B., Blodow, N., Marton, Z. C., and Beetz, M. Aligning point cloud views using persistent feature histograms. In *2008 IEEE/RSJ international conference on intelligent robots and systems*, pp. 3384–3391. IEEE, 2008.

Rusu, R. B., Blodow, N., and Beetz, M. Fast point feature histograms (fpfh) for 3d registration. In *2009 IEEE international conference on robotics and automation*, pp. 3212–3217. IEEE, 2009.

Salas-Moreno, R. F., Newcombe, R. A., Strasdat, H., Kelly, P. H., and Davison, A. J. Slam++: Simultaneous localisation and mapping at the level of objects. In *Proceedings of the IEEE conference on computer vision and pattern recognition*, pp. 1352–1359, 2013.

Sarode, V., Li, X., Goforth, H., Aoki, Y., Srivatsan, R. A., Lucey, S., and Choset, H. Pernet: Point cloud registration network using pointnet encoding. *arXiv preprint arXiv:1908.07906*, 2019.

Thomas, H., Qi, C. R., Deschaud, J.-E., Marcotegui, B., Goulette, F., and Guibas, L. J. Kpconv: Flexible and deformable convolution for point clouds. In *Proceedings of the IEEE/CVF International Conference on Computer Vision*, pp. 6411–6420, 2019.

Tombari, F., Salti, S., and Di Stefano, L. Unique shape context for 3d data description. In *Proceedings of the ACM workshop on 3D object retrieval*, pp. 57–62, 2010.

Vaswani, A., Shazeer, N., Parmar, N., Uszkoreit, J., Jones, L., Gomez, A. N., Kaiser, Ł., and Polosukhin, I. Attention is all you need. In *Advances in neural information processing systems*, pp. 5998–6008, 2017.

Wang, Y. and Solomon, J. M. Deep closest point: Learning representations for point cloud registration. In *Proceedings of the IEEE/CVF International Conference on Computer Vision*, pp. 3523–3532, 2019a.

Wang, Y. and Solomon, J. M. Prnet: Self-supervised learning for partial-to-partial registration. *arXiv preprint arXiv:1910.12240*, 2019b.

Wang, Y., Sun, Y., Liu, Z., Sarma, S. E., Bronstein, M. M., and Solomon, J. M. Dynamic graph cnn for learning on point clouds. *Acm Transactions On Graphics (tog)*, 38(5):1–12, 2019.

Yang, H., Shi, J., and Carlone, L. Teaser: Fast and certifiable point cloud registration. *IEEE Transactions on Robotics*, 37(2):314–333, 2020.

Yang, J., Li, H., Campbell, D., and Jia, Y. Go-icp: A globally optimal solution to 3d icp point-set registration. *IEEE transactions on pattern analysis and machine intelligence*, 38(11):2241–2254, 2015.

Yew, Z. J. and Lee, G. H. 3dfeat-net: Weakly supervised local 3d features for point cloud registration. In *Proceedings of the European Conference on Computer Vision (ECCV)*, pp. 607–623, 2018.

Yew, Z. J. and Lee, G. H. Rpm-net: Robust point matching using learned features. In *Proceedings of the IEEE/CVF conference on computer vision and pattern recognition*, pp. 11824–11833, 2020.

Yu, F. and Koltun, V. Multi-scale context aggregation by dilated convolutions. *arXiv preprint arXiv:1511.07122*, 2015.

Yu, H., Li, F., Saleh, M., Busam, B., and Ilic, S. Cofinet: Reliable coarse-to-fine correspondences for robust point-cloud registration. *Advances in Neural Information Processing Systems*, 34, 2021.

Zeng, A., Song, S., Nießner, M., Fisher, M., Xiao, J., and Funkhouser, T. 3dmatch: Learning local geometric descriptors from rgb-d reconstructions. In *Proceedings of the IEEE conference on computer vision and pattern recognition*, pp. 1802–1811, 2017.

Zhang, J. and Singh, S. Visual-lidar odometry and mapping: Low-drift, robust, and fast. In *2015 IEEE International Conference on Robotics and Automation (ICRA)*, pp. 2174–2181. IEEE, 2015.

Zhao, H., Jiang, L., Jia, J., Torr, P. H., and Koltun, V. Point transformer. In *Proceedings of the IEEE/CVF International Conference on Computer Vision*, pp. 16259–16268, 2021.

Zhou, Q.-Y., Park, J., and Koltun, V. Open3d: A modern library for 3d data processing. *arXiv preprint arXiv:1801.09847*, 2018.

Zhu, L., Liu, D., Lin, C., Yan, R., Gómez-Fernández, F., Yang, N., and Feng, Z. Point cloud registration using representative overlapping points. *arXiv preprint arXiv:2107.02583*, 2021.

## A. Appendix

In this supplementary material, we first introduce evaluation metrics in details in A.1. Then we provide additional results and analysis in A.2. Finally, we show qualitative registration visualizations on 3DMatch, 3DLoMatch, Odometry KITTI and MVP-RG in A.3, and some badcases in A.4.

### A.1. Evaluation metrics

#### A.1.1. 3DMATCH AND 3DLOMATCH

**Inlier Ratio (IR)** measures the proportion of correct correspondences among all the putative correspondences. Consider the putative correspondences  $(\mathbf{x}_i, \mathbf{y}_j) \in \mathcal{C}_{ij}$  retrieved by mutual feature matching, inlier ratio counts the fraction of correct correspondences under the ground truth transformation  $T^*$ :

$$\text{IR} = \frac{1}{|\mathcal{C}_{ij}|} \sum_{(\mathbf{x}_i, \mathbf{y}_j) \in \mathcal{C}_{ij}} [\|T^*(\mathbf{x}_i) - \mathbf{y}_j\|_2 < \tau_1], \quad (\text{A.1})$$

[.] denotes the Iverson bracket and  $\tau_1 = 0.1\text{m}$  which is pre-defined during evaluation.

**Feature Matching Recall (FMR)** measures the percentage of the inlier ratio that is above a certain threshold ( $\tau_2 = 5\%$ ), indicating the pair that is likely to be matched correctly by using some robust estimator such as RANSAC (Fischler & Bolles, 1981):

$$\text{IR} > \tau_2. \quad (\text{A.2})$$

**Registration Recall (RR)** indicates the proportion of successful aligned scan pairs, which directly evaluates the quality of the pairwise registration. Specifically, consider the ground truth correspondence set  $(\mathbf{x}_i, \mathbf{y}_j) \in \mathcal{C}_{ij}^*$ , it computes the root mean square error among  $\mathcal{C}_{ij}^*$  under the predicted transformation  $T$ :

$$\text{RMSE} = \sqrt{\frac{1}{|\mathcal{C}_{ij}^*|} \sum_{(\mathbf{x}_i, \mathbf{y}_j) \in \mathcal{C}_{ij}^*} \|T(\mathbf{x}_i) - \mathbf{y}_j\|_2^2}, \quad (\text{A.3})$$

and calculates the fraction of alignments with  $\text{RMSE} < 0.2\text{m}$ .

#### A.1.2. ODOMETRY KITTI

**Relative Translation Error (RTE)** calculates the Euclidean distance between estimated translation  $t$  and the ground truth translation  $t^*$ :

$$\text{RTE} = \|t - t^*\|_2. \quad (\text{A.4})$$

**Relative Rotation Error (RRE)** measures the discrepancy between the estimated rotation  $R$  and the ground truth rotation matrix  $R^*$ :

$$\text{RRE} = \arccos \left( \frac{\text{trace}(R^{*T} R) - 1}{2} \right), \quad (\text{A.5})$$

where  $\text{trace}(\cdot)$  denotes the trace of the matrix.

**Registration Recall (RR)** measures the proportion of successful aligned scan pairs with both RRE and RTE below a certain threshold:

$$\begin{aligned} \text{RTE} &< 2\text{m}, \\ \text{RRE} &< 5^\circ. \end{aligned} \quad (\text{A.6})$$

It's noted that the final RTE and RRE are both averaged on the successful point cloud pairs.

#### A.1.3. MVP-RG

**Rotation Error** is defined the same as that in Odometry KITTI dataset. To keep up with the symbols in MVP-RG dataset, we use  $\mathcal{L}_R$  instead of RRE to represent the rotation error.

Table A1. GPU memory consumption of PPF

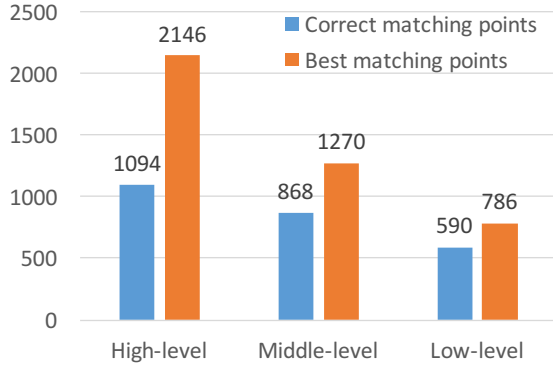
Points	# points	$k$	$D_p$	Memory (MB)
original points	37001 (avg)	1024	64	9,250
<i>superpoints</i>	679 (avg)	64	64	10
original points	60000 (max)	1024	64	15,000
<i>superpoints</i>	1389 (max)	64	64	22
original points	37001 (avg)	1024	256	37001
<i>superpoints</i>	679 (avg)	64	256	40
original points	60000 (max)	1024	256	60,000
<i>superpoints</i>	1389 (max)	64	256	43

**Translation Error** is also defined the same as that in Odometry KITTI dataset. Here we use  $\mathcal{L}_t$  to represent the translation error.

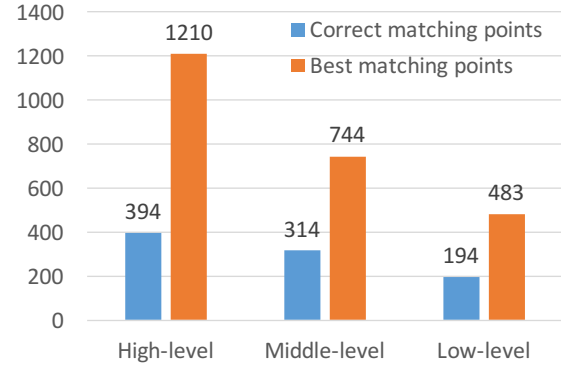
**RMSE** indicates the point-wise distance under the estimated and ground truth transformation:

$$\mathcal{L}_{RMSE} = \frac{1}{N} \sum_{i=1}^N \|T^*(\mathbf{x}_i) - T(\mathbf{x}_i)\|_2, \quad (\text{A.7})$$

where  $N$  denotes the number of points in source point cloud.



(a) 3DMatch (3509 / 5000 overlapping points)



(b) 3DLoMatch (2218 / 5000 overlapping points)

Figure A1. Multi-level features comparison on 3DMatch and 3DLoMatch.

## A.2. Additional results and analysis

### A.2.1. PPF MEMORY ANALYSIS

We compared the GPU memory consumption of PPF on the original points and the *superpoints* on 3DMatch train set. We first calculated the average and maximum points number of the original points and *superpoints*. Then, following PPFNet (Deng et al., 2018b), neighborhood points number  $k$  under the specific radius was set to 1024 for original points, while  $k$  was set to 64 in NgeNet for *superpoints*. The channels number for encoding PPF was marked as  $D_p$ , where 64 and 256 were considered. The GPU memory consumption for the feature map (without considering gradient map or others) is shown in Table A1. GPU memory consumption of PPF on *superpoints* is three orders of magnitude smaller than on original points.

### A.2.2. MULTI-LEVEL FEATURES COMPARISON

We conducted experiments to statistically analyze the distinctiveness of features across all three levels. Considered  $\mathbf{x}_i$  and its corresponding point  $\mathbf{y}_j$ , we found the nearest corresponding points  $\mathbf{y}^l, \mathbf{y}^m, \mathbf{y}^h$  by calculating Euclidean distance in the

relevant feature space respectively. We calculated

$$d_{j_l} = \|\mathbf{y}^l - \mathbf{y}_j\|_2, d_{j_m} = \|\mathbf{y}^m - \mathbf{y}_j\|_2, d_{j_h} = \|\mathbf{y}^h - \mathbf{y}_j\|_2. \quad (\text{A.8})$$

If  $d_{j_q} < 2 \cdot v$ , we regarded that  $\mathbf{x}_i$  belongs to *correct matching points* in level  $q$  ( $q \in \{l, m, h\}$ ), where  $v$  denotes initial voxel size for  $\mathbf{X}$  and  $\mathbf{Y}$ . And we regarded  $\mathbf{x}_i$  belongs to *best matching points* in level  $q$  if  $d_{j_q}$  is the minimal value among  $d_{j_l}, d_{j_m}$  and  $d_{j_h}$ . We counted the average number of *correct matching points* and *best matching points* in different levels separately. The statistical histogram on 3DMatch and 3DLoMatch are illustrated in Figure A1. 5000 points were sampled for feature matching based on overlap and saliency scores, where 3509 and 2218 points were overlapping point averaged on 3DMatch and 3DLoMatch.

By comparing the blue bar chart in Figure A1(a), we conclude that high level features are better than middle and low level features for matching, while middle and low level features can still be used to help finding the correct corresponding points for considerable number of points. By comparing the orange bar chart, we conclude that nearly half number of *best matching points* use high-level features to find the optimal candidate point. However, by using middle and low level features, there are still nearly the same number (1270 + 786) of points in  $\mathbf{X}$  can get the *best* corresponding points in  $\mathbf{Y}$ . Similar results are shown in Figure A1(b). In short, both middle and low level features are useful for matching.

Table A2. Detailed results on the 3DMatch and 3DLoMatch datasets.

3DMatch												3DLoMatch											
Kitchen	Home 1	Home 2	Hotel 1	Hotel 2	Hotel 3	Study	MIT Lab	Avg.	STD	Kitchen	Home 1	Home 2	Hotel 1	Hotel 2	Hotel 3	Study	MIT Lab	Avg.	STD				
# Sample																							
449	106	159	182	78	26	234	45	160	128	524	283	222	210	138	42	237	70	216	140				
Registration Recall (%) $\uparrow$																							
3DSN	90.6	90.6	65.4	89.6	82.1	80.8	68.4	60.0	78.4	11.5	51.4	25.9	44.1	41.1	30.7	36.6	14.0	20.3	33.0	11.8			
FCGF	98.0	94.3	68.6	96.7	91.0	84.6	76.1	71.1	85.1	11.0	60.8	42.2	53.6	53.1	38.0	26.8	16.1	30.4	40.1	14.3			
D3Feat	96.0	86.8	67.3	90.7	88.5	80.8	78.2	64.4	81.6	10.5	49.7	37.2	47.3	47.8	36.5	31.7	15.7	31.9	37.2	10.6			
PREDATOR	97.6	97.2	74.8	<b>98.9</b>	<b>96.2</b>	88.5	85.9	73.3	89.0	9.6	71.5	58.2	60.8	77.5	64.2	61.0	45.8	39.1	59.8	11.7			
CoFiNet	96.4	<b>1.00</b>	76.1	97.8	89.7	84.6	<b>90.2</b>	80.0	89.4	8.1	76.5	63.8	64.9	81.3	59.9	63.4	53.8	<b>73.9</b>	67.2	<b>8.6</b>			
NgeNet	<b>98.9</b>	98.1	<b>81.1</b>	97.8	<b>96.2</b>	88.5	<b>86.7</b>	<b>92.9</b>	<b>6.2</b>	<b>82.8</b>	<b>74.6</b>	<b>69.4</b>	<b>86.7</b>	<b>67.4</b>	<b>71.4</b>	<b>57.4</b>	<b>65.7</b>	<b>71.9</b>	8.8				
Relative Rotation Error (°) $\downarrow$																							
3DSN	1.926	1.843	2.324	2.041	1.952	2.908	2.296	2.301	2.199	0.321	3.020	3.898	3.427	3.196	3.217	3.328	4.325	3.814	3.528	0.414			
FCGF	1.767	1.849	2.210	1.867	1.667	2.417	2.024	<b>1.792</b>	<b>1.949</b>	0.236	2.904	3.229	3.277	2.768	2.801	2.822	3.372	4.006	3.147	0.394			
D3Feat	2.016	2.029	2.425	1.990	1.967	2.400	2.346	2.115	2.161	<b>0.183</b>	3.226	3.492	3.373	3.330	3.165	2.972	3.708	3.619	3.361	<b>0.227</b>			
PREDATOR	1.861	1.806	2.473	2.045	<b>1.600</b>	2.458	<b>2.067</b>	1.926	2.029	0.286	3.079	2.637	<b>3.220</b>	2.694	2.907	3.390	<b>3.046</b>	3.412	<b>3.048</b>	0.273			
CoFiNet	1.986	1.777	2.213	1.982	1.820	<b>1.709</b>	2.575	1.956	2.002	0.261	3.097	2.946	3.488	2.750	3.009	3.462	4.123	3.293	3.271	0.401			
NgeNet	<b>1.679</b>	<b>1.699</b>	<b>2.166</b>	<b>1.501</b>	1.665	2.371	2.145	1.869	2.115	0.286	<b>2.507</b>	<b>2.635</b>	3.278	<b>2.492</b>	<b>2.601</b>	<b>2.755</b>	3.204	<b>3.050</b>	3.264	0.296			
Relative Translation Error (m) $\downarrow$																							
3DSN	0.059	0.070	0.079	0.065	0.074	0.062	0.093	0.065	0.071	<b>0.010</b>	0.082	0.098	0.096	0.101	<b>0.080</b>	0.089	0.158	0.120	0.103	0.024			
FCGF	0.053	0.056	0.071	0.062	0.061	0.055	0.082	0.090	0.066	0.013	0.084	0.097	<b>0.076</b>	0.101	0.084	0.077	0.144	0.140	0.100	0.025			
D3Feat	0.055	0.065	0.080	0.064	0.078	0.049	0.083	0.064	0.067	0.011	0.088	0.101	0.086	0.099	0.092	0.075	0.146	0.135	0.103	0.023			
PREDATOR	0.048	<b>0.055</b>	0.070	0.073	0.060	0.065	<b>0.080</b>	<b>0.063</b>	<b>0.064</b>	<b>0.010</b>	0.081	0.080	0.084	0.099	0.096	0.077	<b>0.101</b>	0.130	0.093	0.016			
CoFiNet	0.049	0.059	0.064	0.065	0.066	<b>0.045</b>	0.089	0.074	<b>0.064</b>	0.013	0.079	<b>0.076</b>	0.087	0.086	0.085	0.074	0.139	0.094	<b>0.090</b>	0.020			
NgeNet	<b>0.042</b>	0.057	<b>0.060</b>	<b>0.057</b>	<b>0.058</b>	0.059	0.083	0.073	0.073	0.011	<b>0.070</b>	0.079	0.085	<b>0.078</b>	0.088	<b>0.063</b>	0.103	<b>0.083</b>	0.096	<b>0.011</b>			

### A.2.3. SCENE PERFORMANCE ON 3DMATCH AND 3DLOMATCH

We report *Registration Recall* (RR) on 3DMatch and 3DLoMatch in scene level, with additional evaluation metrics including *Relative Rotation Error* (RRE) and *Relative Translation Error* (RTE). The results are shown in Table A2. Successfully registered pairs in each scene are included to calculate RRE and RTE. We achieve the highest RR in most scenes and the second highest in few scenes. Despite significant improvement has been made in RR, which indicates taking more difficult pairs into account, there is a slight growth in RRE and RTE. It shows NgeNet is robust and accurate for registration.

### A.2.4. PAIR RECALL ON 3DMATCH

Scene RR is our previous reported RR which calculates the average registration recall across scenes. However, the unbalanced sample numbers in each scene may be unfair for scene RR metrics. Here, we additionally report pair RR on 3DMatch, which calculates the average RR among all 1279 pairs without taking scene category into consideration. The results are summarized in Table A3. Both scene RR and pair RR are improved with the proposed modules.

Table A3. Ablation study on 3DMatch dataset.

base	ms	voting	GGE	scene RR (%) $\uparrow$	pair RR (%) $\uparrow$
✓				89.3	91.2
✓	✓			90.3	92.2
✓	✓	✓		91.5	93.1
✓			✓	91.2	92.8
✓	✓	✓	✓	<b>92.9</b>	<b>94.1</b>

#### A.2.5. SALIENCY LOSS

The ground truth labels  $\bar{\mathbf{S}}_{\mathbf{X}} \in \mathbb{R}^N$ ,  $\bar{\mathbf{S}}_{\mathbf{Y}} \in \mathbb{R}^M$  for saliency loss are obtained on the fly with feature matching. For  $\bar{\mathbf{S}}_{\mathbf{X}}$ , feature matching is conducted based on  $\mathbf{F}_{\mathbf{X}}^h$  and  $\mathbf{F}_{\mathbf{Y}}^h$  as follows:

$$\mathbf{M} = \mathbf{F}_{\mathbf{X}}^h \cdot (\mathbf{F}_{\mathbf{Y}}^h)^T. \quad (\text{A.9})$$

For point  $\mathbf{x}_i$ , the corresponding point index in  $\mathbf{Y}$  is obtained by  $j = \arg \max \mathbf{M}[i, :]$ . If  $(\mathbf{x}_i, \mathbf{y}_j)$  belongs to correspondences set under the ground truth transformation,  $\bar{\mathbf{S}}_{\mathbf{X}_i}$  is set to 1, otherwise set to 0.

It's noticed that  $\mathbf{M} \in \mathbb{R}^{N \times M}$  (in 3DMatch and Odometry KITTI) is huge matrix where  $N$  and  $M$  are about in tens of thousands level. We ablated the saliency loss on 3DMatch dataset, and the results<sup>2</sup> can be seen in Table A4. Saliency loss slightly improves the performance but brings huge additional memory consumption. Removing saliency loss is an option when we train point clouds with more points in the future and slight performance degradation is allowed.

Table A4. Performance on 3DMatch w/wo saliency loss under 5000 sampling points.

Saliency loss	IR (%) $\uparrow$	FMR (%) $\uparrow$	scene RR (%) $\uparrow$	pair RR (%) $\uparrow$	Memory (MB) $\downarrow$
wo	62.4	<b>98.4</b>	92.4	93.6	<b>3723</b>
w	<b>63.1</b>	98.2	<b>92.9</b>	<b>94.1</b>	6646

#### A.3. Qualitative results of registration

Qualitative registration results on 3DMatch, 3DLoMatch, Odometry KITTI and MVP-RG are shown in Figure A2.

#### A.4. Bad cases visualization

Some bad registration results on 3DMatch, 3DLoMatch, Odometry KITTI and MVP-RG can be seen in Figure A3.

<sup>2</sup>Memory is obtained using function `torch.cuda.max_memory_allocated()` in PyTorch.

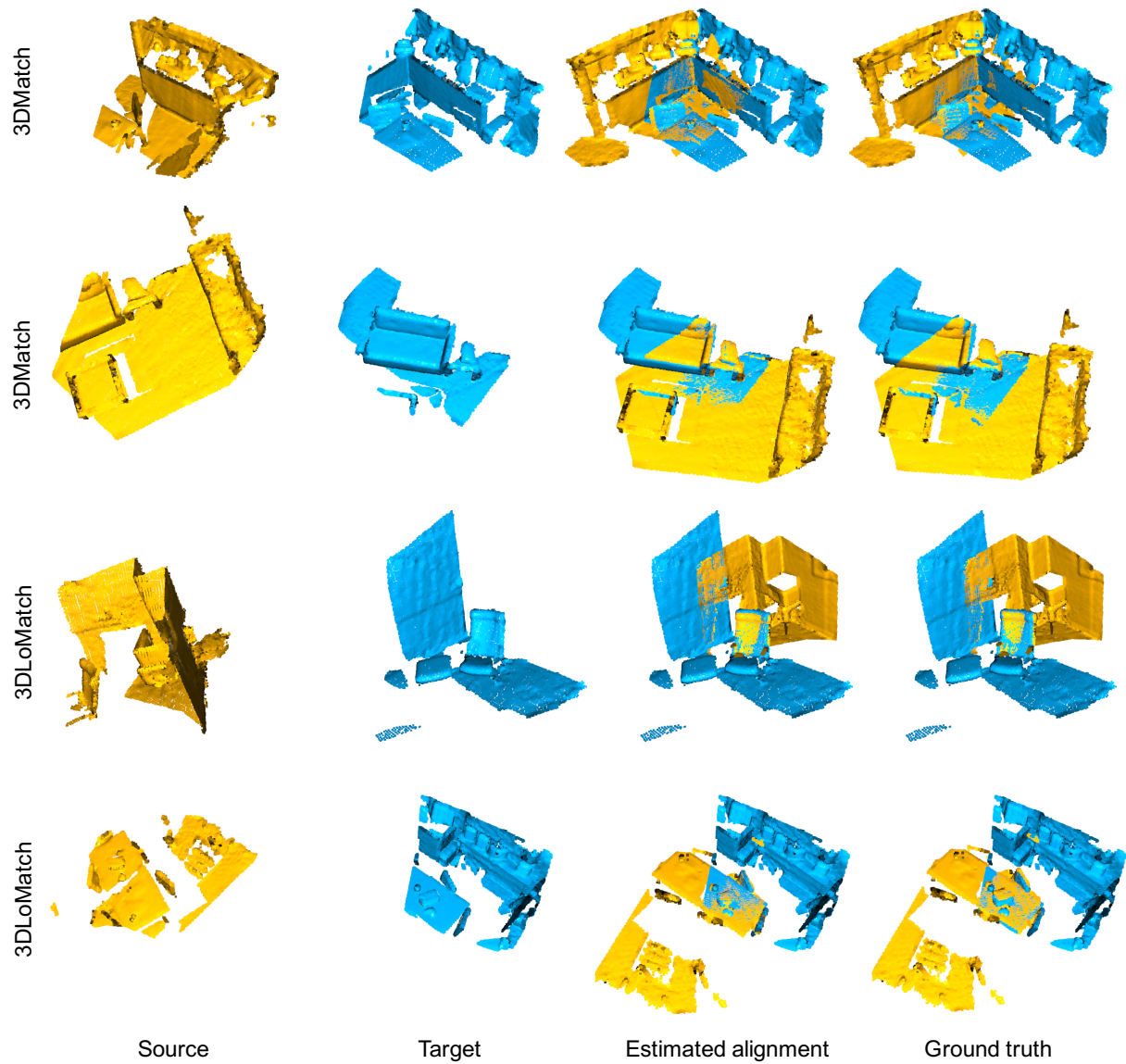


Figure A2. Registration visualization on 3DMatch, 3DLoMatch, Odometry KITTI and MVP-RG.

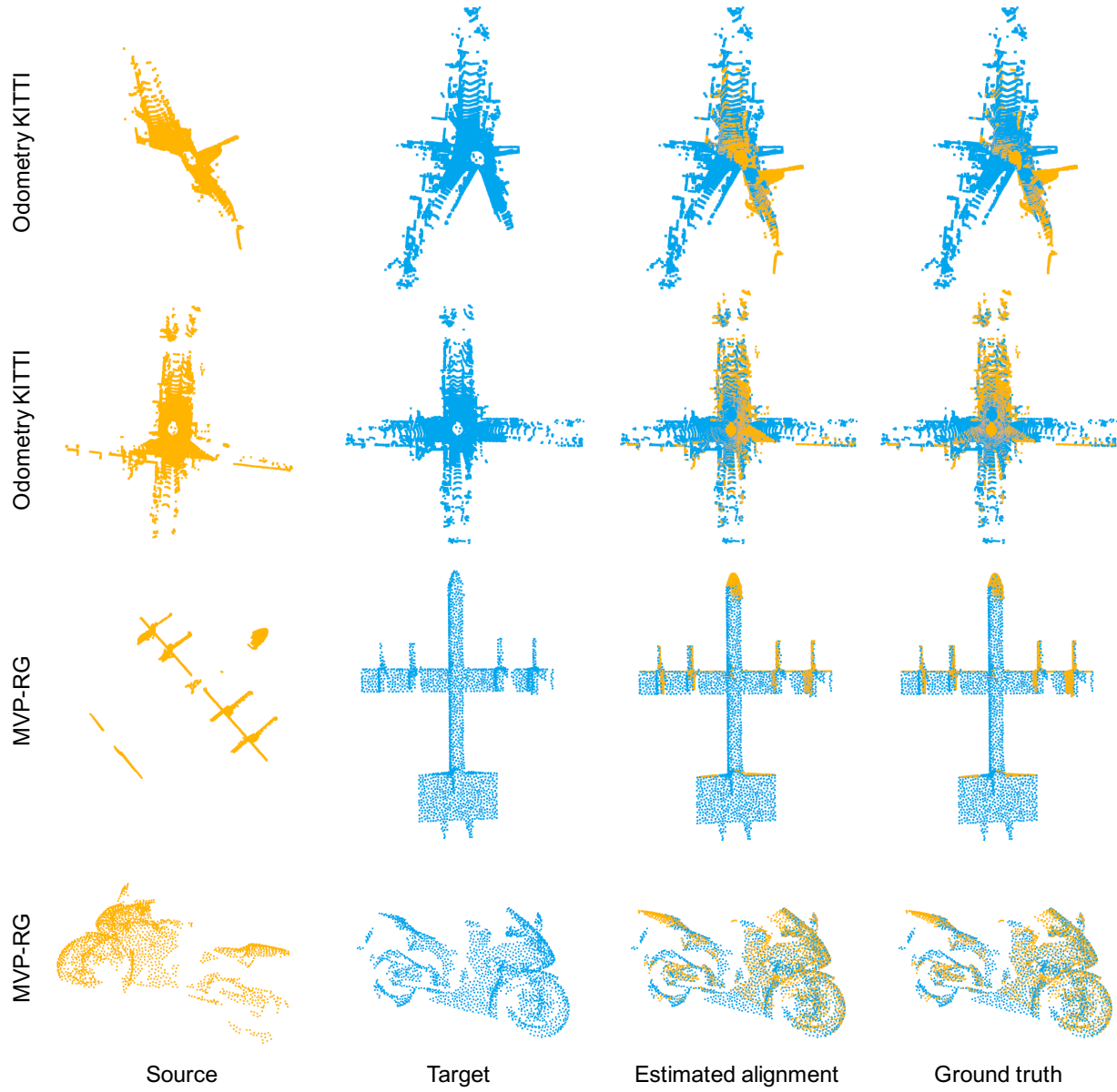


Figure A2. Registration visualization on 3DMatch, 3DLoMatch, Odometry KITTI and MVP-RG.

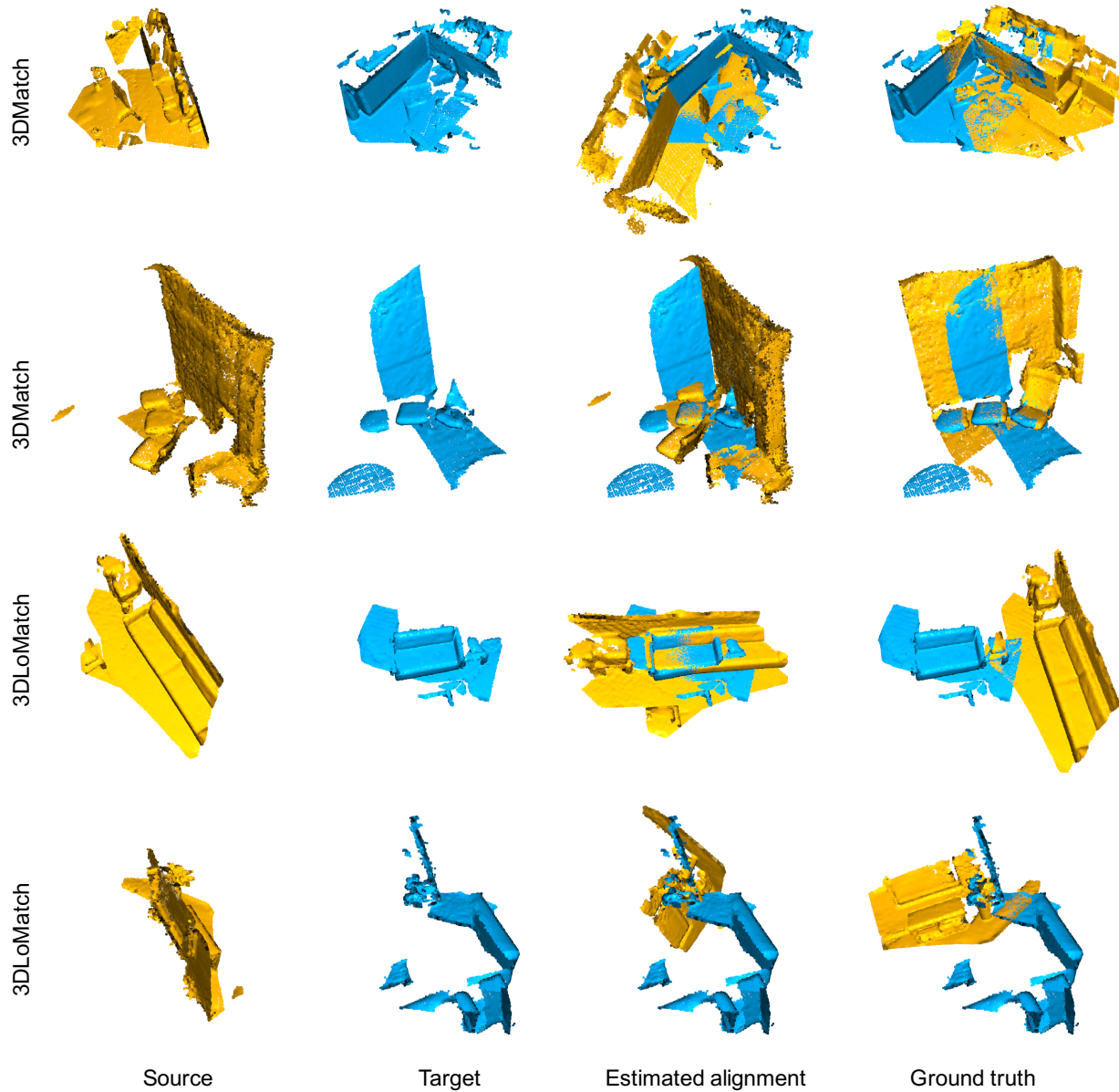


Figure A3. Bad cases registration visualization on 3DMatch, 3DLoMatch, Odometry KITTI and MVP-RG.

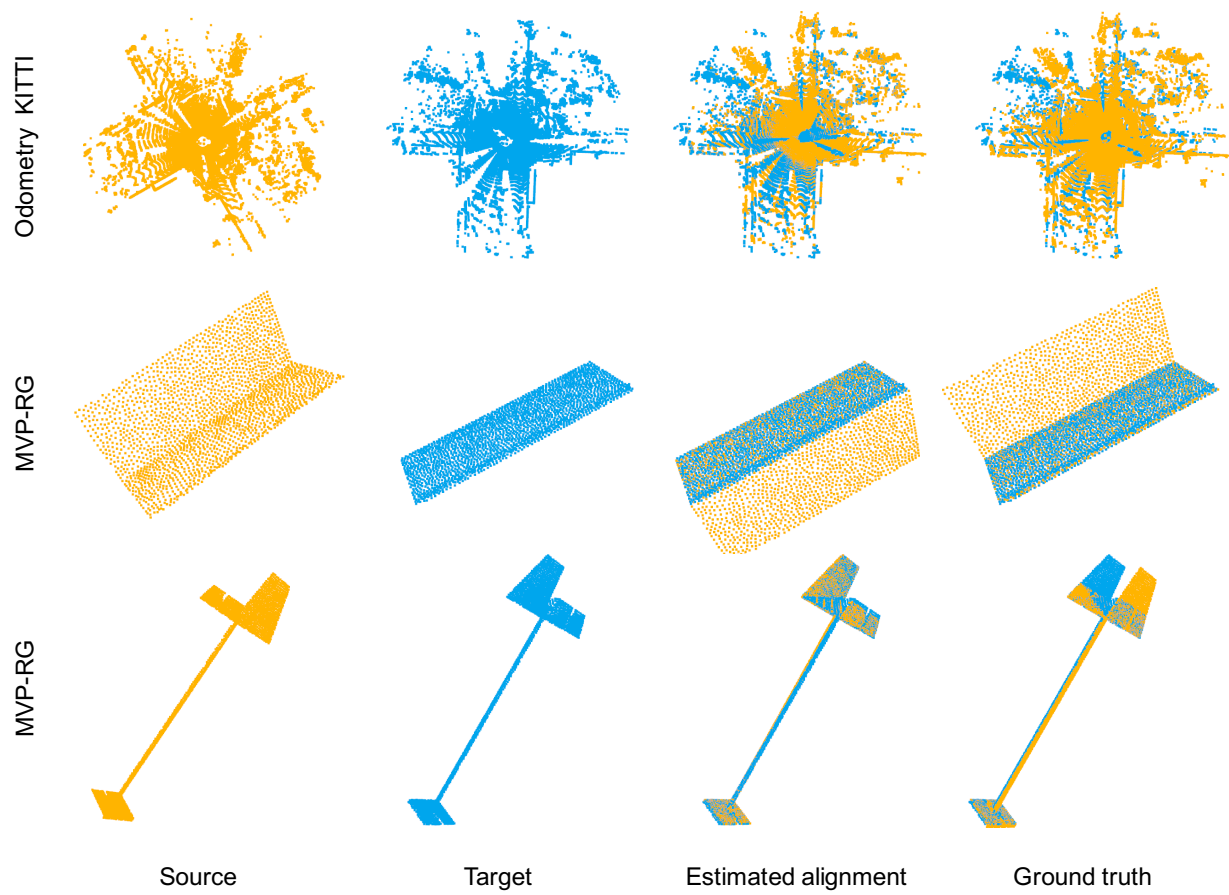


Figure A3. Bad cases registration visualization on 3DMatch, 3DLoMatch, Odometry KITTI and MVP-RG.